# Strongly Coupled Plasmon and Phonon Polaritons as Seen by Photon and Electron Probes

Pavel Gallina,[1,2] Andrea Konečná,[1,*] Jiří Liška,[1] Juan Carlos Idrobo,[3] and Tomáš Šikola[1,2]

[1] *Central European Institute of Technology, Brno University of Technology, Brno 612 00, Czech Republic*
[2] *Institute of Physical Engineering, Brno University of Technology, Brno 616 69, Czech Republic*
[3] *Materials Science and Engineering Department, University of Washington, Seattle, Washington 98195, USA*

(Received 12 November 2022; revised 22 December 2022; accepted 23 December 2022; published 15 February 2023)

The ability to control and modify infrared excitations in condensed matter is of both fundamental and applied interest. Here we explore a system supporting low-energy excitations, in particular, mid-infrared localized plasmon modes and phonon polaritons that are tuned to be strongly coupled. We study the coupled modes by using far-field infrared spectroscopy, state-of-the-art monochromated electron energy-loss spectroscopy, numerical simulations, and analytical modeling. We demonstrate that the electron probe facilitates a precise characterization of polaritons constituting the coupled system, and enables an active control over the coupling and the resulting sample response both in frequency and space. Although far-field optical spectra can be substantially different from near-field electron energy-loss spectra, we show that a direct comparison is possible via postprocessing and right positioning of the electron beam. The resulting spectra allow us to evaluate the key parameters of the coupled system, such as the coupling strength, which we demonstrate to be probe independent. Our work establishes a rigorous description of the spectral features observed in light- and localized electron-based spectroscopies, which can be extended to the analysis of analogous optical systems with applications in heat management and electromagnetic field concentration or nanofocusing.

DOI: 10.1103/PhysRevApplied.19.024042

## I. INTRODUCTION

Polaritons are quasiparticles emerging due to strong coupling between photons and excitations in condensed matter, such as plasmons in metals and semiconductors or optical phonons in ionic crystals [1]. The resulting plasmon polaritons (PPs) and phonon polaritons (PhPs) are known to facilitate the confinement of light at the nanoscale, often deeply below the diffraction limit, which finds applications in nanoscale focusing [2–5], extreme waveguiding [6], the design of optical elements [7], or enhanced molecular detection [8]. Spatial confinement and energies of the polaritonic excitations can be typically tuned by nanostructuring, e.g., in a form of gratings or the so-called optical nanoantennas [9], but also by coupling between polaritons themselves. Such coupling results in hybridized modes [10–15] and introduces more degrees of freedom to engineer system functionalities and on-demand optical response [16,17],

Both uncoupled and coupled polaritons in the mid-infrared (MIR) energy range have been experimentally explored by far-field IR spectroscopy [18–21]. IR spectroscopy provides very high spectral resolution; however, its spatial resolution is restricted by the diffraction limit. Accessing both spectral and spatial information on the coupled polaritonic modes is only possible by utilizing near-field probes. Besides scanning near-field optical microscopy [22], which relies on light localized at sharp tips, we can nowadays employ focused fast electron beams. Only very recently, due to instrumental improvements [23], electron energy-loss spectroscopy (EELS) [24] in a scanning transmission electron microscope (STEM) has become another suitable technique for mapping MIR polaritons with (sub)nanometric spatial and few-millielectronvolt spectral resolution [25–32].

Coupled polaritonic systems have so far been analyzed by one of the aforementioned experimental techniques; however, a correlative study that would bring detailed understanding of common aspects and differences between spectral features measured by light- or electron-based spectroscopic techniques in the same sample is, to the best of our knowledge, missing. In this work, we present such a correlative study and explore nanostructured systems, where both infrared PhPs and PPs can exist. We probe the electromagnetic coupling between MIR surface PhPs (SPhPs) in a thin silicon dioxide film and low-energy localized surface plasmon (LSP) modes formed by the

---

[*] andrea.konecna@vutbr.cz

confinement of PPs in micrometer-long gold antennas. We find that far-field IR spectra of the coupled LSPs-SPhPs can be substantially different from EEL spectra, which we confirm by experiments supported by numerical simulations and analytical modeling. We show that, by precisely positioning the electron beam, the coupling between the polaritonic excitations can selectively trigger either SPhPs only or coupled LSPs-SPhPs. We also present a postprocessing analysis in the EEL spectra that facilitates identification of the hybrid modes, allowing an easier comparison to far-field optical spectroscopy.

## II. METHODS

### A. Numerical simulations

Finite-difference time-domain simulations of far-field optical spectra are obtained using the Ansys Lumerical software [33]. A single rectangular antenna placed on a semi-infinite membrane is illuminated by a linearly polarized plane wave impinging at normal incidence with respect to the substrate provided by a total-field–scattered-field (TFSF) source. The scattering (absorption) spectra are calculated from the scattered (total) power flux monitors placed outside (inside) the TFSF source. The whole simulation domain with dimensions of 10 μm × 10 μm × 6 μm is enclosed in a perfectly matched layer.

EEL spectra and field plots are obtained using the finite-element method implemented within the COMSOL Multiphysics® software [34], where we calculate the induced electromagnetic field emerging in the interaction of the nanostructure with a line current representing the focused electron probe. The EEL probability is then evaluated as [35]

$$\Gamma(\mathbf{R}_b,\omega)=\frac{e}{\pi\hbar\omega}\int_{-\infty}^{\infty}dz\,\mathrm{Re}\{E_z^{\mathrm{ind}}(\mathbf{R}_b,z,\omega)\,e^{-i\omega z/v}\},\quad (1)$$

where $e$ is the elementary charge, $\hbar\omega$ energy, and $v$ the electron velocity; $z$ denotes the optical axis along which the fast electron propagates, $\mathbf{R}_b=(x_b,y_b)$ is the impact parameter (i.e., position in the transverse plane with respect to the optical axis that the electron trajectory intersects), and we integrate the $z$ component of the induced electric field along the beam trajectory.

### B. Experimental methods

Electron-beam lithography on $SiO_2$ TEM membranes (thickness 40 nm) is performed using a scanning electron microscope Mira3 (Tescan) with a laser interferometry stage (Raith). Subsequent gold deposition is done using an electron-beam evaporator (Bestec).

Fourier-transform infrared spectroscopy (FTIR) is performed with an IR microscope [Vertex 70v and an IR microscope Hyperion 3000 (Bruker)] with an aperture allowing signal collection from an area of 50 μm × 50 μm in a spectral range of $600-6000\ \mathrm{cm}^{-1}$ and resolution of $2\ \mathrm{cm}^{-1}$. Convergence (illumination) and collection semiangles are between 15° and 30°.

Electron energy-loss spectra are acquired using a Nion monochromated aberration-corrected scanning transmission electron microscope operated at 60 kV accelerating voltage [23,36]. The measurements are performed with a convergence semiangle of 30 mrad, a collection semiangle of 20 mrad, a beam current of about 20 pA, using a Nion Iris spectrometer with a dispersion of 0.4 meV/channel [37], and an energy resolution [defined as the full width at half maximum (FWHM) of the zero loss peak] between 10 and 14 meV.

## III. RESULTS AND DISCUSSION

### A. Response of uncoupled system constituents

To understand the spectral response of the studied nanostructured system, we first theoretically analyze the response of its individual constituents, i.e., a $SiO_2$ film and a long Au antenna, when they are excited by light and by a focused electron probe in Fig. 1. The optical response of $SiO_2$ in the spectral region of interest is governed by a phononic mode corresponding to the Si-O-Si symmetric stretching vibration around 100 meV and a mode stemming from the Si-O-Si antisymmetric stretch around 130 meV [38]. The latter mode is associated with strong polarization, yielding the transverse optical–longitudinal optical (TO-LO) splitting associated with the energy region, known as the Reststrahlen band (RB), where $\mathrm{Re}[\epsilon_{\mathrm{SiO}_2}]<0$, which forbids propagation of light within the bulk. However, in the presence of boundaries, such as those imposed in the thin-film geometry, interface SPhPs emerge inside the RB [40].

Because of the energy-momentum mismatch, infrared photons cannot excite SPhPs in a thin film, as demonstrated in Fig. 1(a). The most intense spectral feature corresponds to the excitation of the TO phonons that yields a strong absorption (red line) and featureless field profile (not shown). The absorption spectrum is nearly equal to extinction (scattering is negligible) and thus proportional to $\mathrm{Im}[\epsilon_{\mathrm{SiO}_2}]$.

Focused fast electrons, on the other hand, can provide sufficient momentum and naturally excite the SPhPs inside the RB, as shown by the green spectrum in Fig. 1(a), consistent with recent experiments [27,41,42]. More precisely, fast electrons interacting with a thin film supporting polaritons can excite either charge-symmetric or charge-antisymmetric SPhP modes [9,43] [see the inset in (a)]. SPhPs in $SiO_2$ are rather damped compared especially to those in ionic crystals [22,25], resulting in the two SPhP modes being spectrally indistinguishable. However, due to the symmetry of the probing field, the main peak close to 140 meV is dominated by charge-symmetric SPhPs, as shown schematically in the inset and further confirmed in

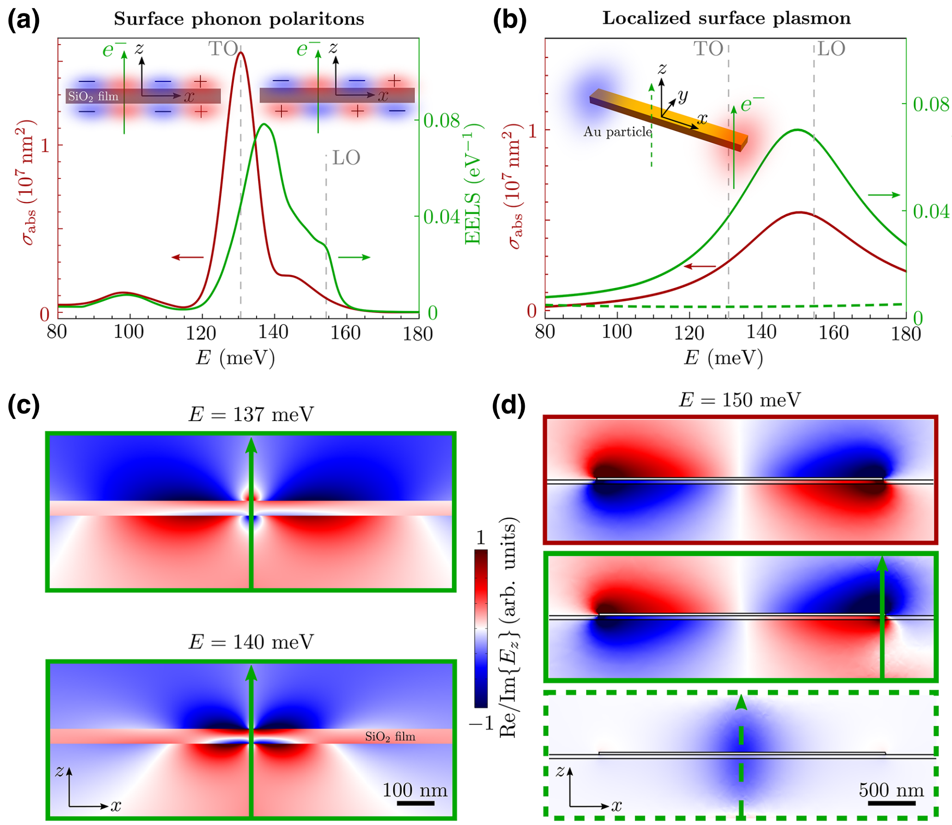

FIG. 1. (a) Numerically calculated EEL (green) and optical absorption (red) spectra of an infinitely extended SiO$_2$ thin film with a thickness of $t = 40$ nm. The dielectric response of SiO$_2$ is modeled using the complex dielectric response obtained from experimental measurements in Ref. [38]. All the spectra are probe-position invariant. Vertical dashed lines denote energies of the TO and LO phonons in SiO$_2$. The inset shows charge-symmetric (left) and charge-antisymmetric (right) SPhP modes. (b) Spectral response of a gold (dielectric response taken from Ref. [39]) rectangular plasmonic antenna with length $L = 3$ μm, width $w = 400$ nm, and height $h = 25$ nm on top of a substrate of thickness $t = 40$ nm with a constant dielectric response (characterized by a relative dielectric constant $\epsilon_{\mathrm{sub}} = 1.8$). Absorption (red line) cross section is calculated for excitation by a plane wave impinging at normal incidence along the $z$ axis with a linear polarization aligned along the long antenna's axis ($x$ axis). EEL spectra are obtained for an electron beam placed 10 nm outside the antenna's corner (solid green line) and at the antenna's center (dashed green line), as shown in the schematics. The electron-beam energy is 60 keV in both (a) and (b). (c) The $z$ component of the total electric field emerging in the excitation of the SiO$_2$ film by focused electrons (trajectories shown by green arrows) at two energies around the peak in the EEL spectrum in (a). (d) The $z$ component of the electric field confirming the excitation of the dipolar plasmon by the plane wave (top red framed plot) and the electron beam placed close to the antenna side (middle green solid framed plot). When the electron beam passes close to the antenna center, it can only weakly excite a higher-order plasmon mode (bottom dashed green framed plot). All plots are obtained at energy 150 meV, approximately corresponding to the peaks in (b), and are extracted at the central plane $y = 0$ while the electron beam is passing in the plane $y_b = d/2 + 10$ nm (10 nm from the antenna's shorter edge). In (c), (d), we show total field in the electron-beam excitation (green frames) and induced field for the plane-wave excitation (red frame). Real part of the field is shown in panels (c) while imaginary part is plotted in (d).

the field plots in (c). The field plots demonstrate that the electron beam couples (with different probability) to SPhPs with varying wavelengths and energies within the entire RB. The fast electrons can also excite the bulk LO phonon, which requires high momentum to be activated, corresponding to the polarization along the electron trajectory. The LO phonon excitation appears as a small "shoulder" close to 155 meV.

To enable an efficient coupling between the different types of polaritons, a spatial overlap of their electromagnetic fields as well as an overlap of their energies needs to be simultaneously targeted. As the SPhPs in SiO$_2$ emerge in the RB between about 130 and 155 meV, we tune the LSP resonances accordingly by a careful choice of the metal used and dimensions of the plasmonic antenna. We consider gold particles of a rectangular shape and numerically simulate their spectral response as if the antenna is probed by a plane wave polarized along its long axis or by a perfectly focused electron beam placed close to the antenna's corner [see the inset in Fig. 1(b)].

For antennas with dimensions $L \times w \times h = 3000 \times 400 \times 25\ \mathrm{nm}^3$ placed on a 40-nm-thick dielectric substrate (mimicking a constant dielectric offset imposed by the $SiO_2$ film), we obtain the theoretical lowest-energy dipolar LSP resonance centered around 150 meV, as shown in Fig. 1(b). The light excitation leads to relatively strong absorption (red line) associated with a dipolar mode that enhances the electric field close to the antenna's tips. The electron beam is also capable of excitation of the same dipolar mode, which is demonstrated in the numerically calculated EEL probability (solid green line). Alternatively, focusing the electrons close to the antenna center results in a near zero signal (dashed green line) in the energy region of interest, since only higher-order modes at larger energies can be excited in this case [44,45]. We confirm these observations in Fig. 1(d), where we plot the electric field in the vicinity of the antenna. For the plane-wave excitation (red-framed plot) and for the electron beam placed close to the antenna side (green framed plot), the field clearly corresponds to the opposite charges accumulated at the left and right sides of the antenna, and thus the dipolar plasmon. The electron beam placed at the antenna center is capable of exciting only a higher-order plasmon and therefore the corresponding plot [dashed green framed plot in Fig. 1(d)] is dominated by the field produced by the electron beam.

### B. Coupled system

From the analysis of the system constituents, we can see that in an uncoupled scenario, the setup consisting of a gold antenna on top of a thin $SiO_2$ film can sustain three dominant polaritonic modes in the energy region of interest: a single LSP mode, and symmetric and antisymmetric thin-film SPhP modes (in formulas abbreviated as $\mathrm{SPhP}_1$ and $\mathrm{SPhP}_2$, respectively). The electromagnetic interaction between these polaritonic modes can be described by a model of three coupled oscillators captured within the matrix

$$\mathbf{M} = \begin{bmatrix} 1/(\alpha_{\mathrm{LSP}} f_{\mathrm{LSP}}) & -K_1 & -K_2 \\ -K_1 & 1/(\alpha_{\mathrm{SPhP}_1} f_1) & 0 \\ -K_2 & 0 & 1/(\alpha_{\mathrm{SPhP}_2} f_2) \end{bmatrix}, \quad (2)$$

where $\alpha_n = 1/[\omega_n^2 - \omega(\omega + i\gamma_n)]$ (here $n = \{\mathrm{LSP}, \mathrm{SPhP}_1, \mathrm{SPhP}_2\}$) determines the spectral response of a mode with a resonant energy $\hbar\omega_n$, damping $\hbar\gamma_n$, and effective strength $f_n$. In the following, we assume that the phononic modes are nonradiative, while the damping of the LSP involves radiative losses, i.e., $\gamma_{\mathrm{LSP}} \rightarrow \gamma_{\mathrm{LSP}} + \omega^2/(6\pi\epsilon_0 c^3)$ [15,46,47]. The coupling will introduce three new hybrid modes whose eigenfrequencies and dampings are obtained from $|\mathbf{M}| = 0$. However, the coupling is efficient only if both spectral and spatial overlaps of the modes' electromagnetic fields are achieved, which is described by the coupling parameters $K_1$ and $K_2$. We also assumed that SPhPs do not couple to each other.

Now we consider the same antenna and thin-film dimensions as in Fig. 1 and analyze optical absorption and scattering spectra of the coupled system [red and blue lines in Fig. 2(a), respectively], which exhibit several spectral features. The absorption is again dominated by the excitation of the TO phonon mode and with a similar spectral behavior as that of pure $SiO_2$ [as shown in Fig. 1(a)], which is due to the large extent of the thin film and the presence of absorption unrelated to the coupling. The scattering, on the other hand, clearly shows excitations beyond the RB as well as an additional weaker peak within the RB. All three peaks are associated with the new hybrid modes emerging due to the coupling. We also empirically find that the experimental measurement of $(1 - T_{\mathrm{rel}})$, where $T_{\mathrm{rel}}$ is the relative transmission obtained from FTIR (orange line), strongly resembles the theoretically predicted scattering spectra with only a slight discrepancy in the positions of the new peaks [see also Fig. 3(b) below and Appendix A].

As previously mentioned, an electron beam allows us to control the strength of the plasmonic excitation by simply positioning the beam at different relative positions from the antenna's center (or tip), as shown in the inset of Fig. 2(b). The corresponding simulated spectra (shown in the figure as thin lines) then capture either only nearly noninteracting SPhPs and bulk LO phonons excited in the $SiO_2$ (black), or a mixture of noninteracting SPhPs and coupled LSP-SPhPs (red to violet). The coupling is clearly manifested by a dip around the TO phonon position and emergence of new peaks beyond the RB. The weaker excitation inside the RB is here indistinguishable due to the presence of the uncoupled SPhP and bulk signal.

Note that the spectrum calculated at the antenna's center is slightly different from that of a plain $SiO_2$ film shown in Fig. 1(a). This happens because the antenna represents an obstacle for the SPhPs and thus favors excitation of SPhPs with slightly different momenta. As faintly observed in the corresponding field plot in Fig. 2(d) at 137 meV, the SPhPs interact with the edges of the antenna.

The experimental EEL spectra plotted in Fig. 2(b) (shown as thick lines) obtained for similar beam positions as in the simulations show less features due to limited energy resolution (between 10 and 14 meV). However, a clear broadening and emergence of "shoulders" of the main peak associated with the polaritonic coupling when the beam approaches the tip of the antenna can still be resolved. Similar behavior of the simulated spectra is obtained when the finite experimental resolution is introduced in the simulations (see Fig. 6 in Appendix B).

In general, the far-field optical spectra of the coupled system are very different to EELS due to the absence of the spectral features corresponding to the nearly uncoupled SPhPs that are not directly excitable by plane waves, but launchable by fast electrons. Interestingly, we can

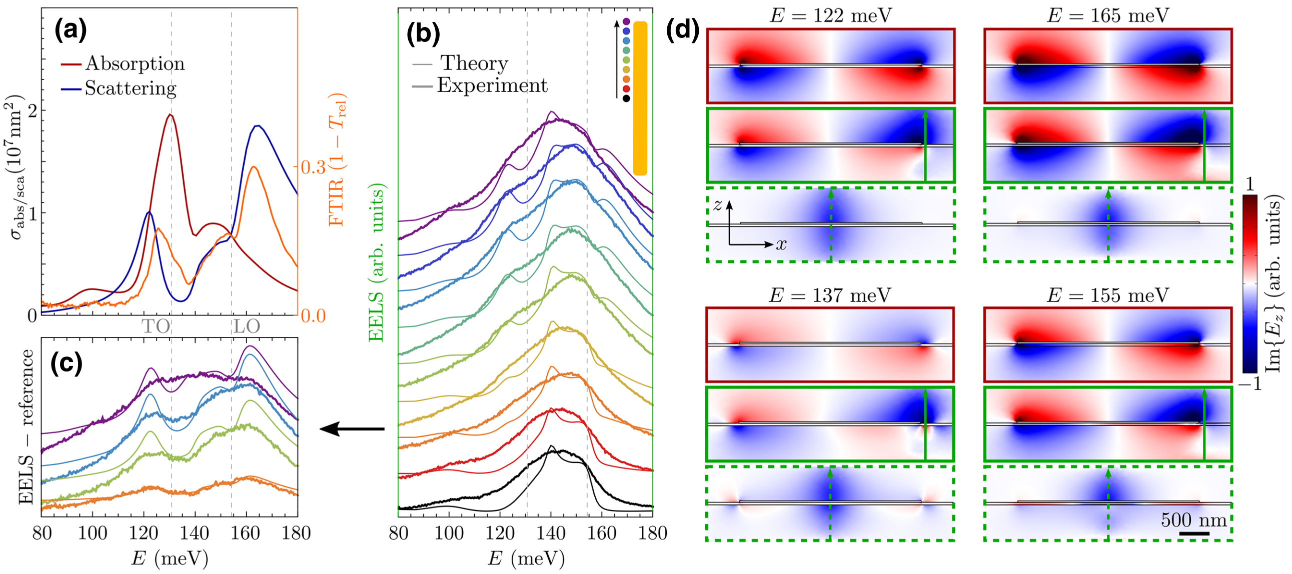

FIG. 2. Comparison of electron and light spectra for an approximately optimally coupled antenna-substrate system (individual system components have the same geometry and dimensions as in Fig. 1). (a) Experimentally measured FTIR spectrum corresponding to $(1 - T_{\rm rel})$, where $T_{\rm rel}$ is the transmission (orange line) for light polarized along the long antenna axis, divided by a reference transmission spectrum on a plain $SiO_2$ layer. Numerically calculated absorption (red) and scattering (blue) cross-section spectra for an entire system are shown for comparison. (b) Experimental versus calculated electron spectra (thick versus thin lines) obtained for the 60-keV beam, which is placed just next to the antenna and scanned along the antenna's long axis. Colors approximately correspond to the electron positions as marked schematically in the inset. (c) Selected EEL spectra from (b) after subtraction of the (reference) spectrum recorded at the center of the antenna, which is dominated by uncoupled SPhPs and LO phonon excitation in $SiO_2$ [black lines in (b)]. For clarity, subsequent spectra in (b) and (c) are vertically shifted by a constant offset. The vertical dashed lines denote energies of TO and LO phonon modes in $SiO_2$. (d) The $z$ component of the electric field for plane-wave and electron excitation (red and blue framed plots, respectively) at different energies as denoted above. The electron beam is placed at the side of the antenna or close to its center (solid versus dashed framed plots; electron trajectories are represented by green lines). All plots are extracted at the central plane $y = 0$ while the electron beam is passing in the plane $y_b = w/2 + 10$ nm (10 nm from the antenna's shorter edge). We show total field in the electron-beam excitation (green frame) and induced field for the plane-wave excitation (red frames).

achieve resemblance between the light and EEL spectral signals by postprocessing of EEL spectra. As only bulk LO phonon and nearly uncoupled SPhPs are excited by the beam at the center of the antenna, we take the black spectrum in Fig. 2(b) as a reference and subtract it from the spectra obtained with the beam positioned at different distances from the antenna tip. Although the directly launched SPhPs for varying beam positions acquire slightly different momenta because of varying distance between the beam and antenna edges at which the polaritons scatter, such subtraction makes the EEL spectra better comparable with optical scattering spectra. See, for instance, the selected spectra in Fig. 2(c). The resulting peak intensities, relative strength, and contrast however change with the beam position, which controls the plasmon mode excitation efficiency. We emphasize that the subtraction also allows clear distinction of the coupling-related spectral signatures for the measured data, which before the subtraction in (b) showed only one broad spectral feature.

Electric field profiles shown in Fig. 2(d) for the plane-wave (red frames) and electron-beam (green frames) excitations are dominated by the presence of the dipolar plasmonic field, except for the cases when the electron beam is passing close the antenna center (dashed green framed plots). Hence, they strongly resemble the field plots in Fig. 1(d) with slight, yet important differences due to the presence of the $SiO_2$ film: (1) depletion versus enhancement of the field inside the $SiO_2$ film beneath the antenna (energies outside the RB; 122 versus 165 meV), and (2) emergence of uncoupled SPhPs freely propagating from the antenna at 137 meV within the RB. Unfortunately, due to the strong damping of the SPhPs, we can only observe one field oscillation [similarly as in Fig. 1(c)] near the antenna boundaries and close to the electron beam. We also note that the directly launched SPhPs strongly contribute to EEL spectra [black line in Fig. 2(b)] as they couple to the electron beam, while for plane-wave excitation, we only observe a small contribution from the SPhPs launched secondarily by the antenna (faint features close to the antenna sides appearing in the plot at 137 meV).

## IV. CONTROLLING THE COUPLING

The coupling can be adjusted by tuning the LSP energies, as shown in many preceding studies [8,14,28,45].

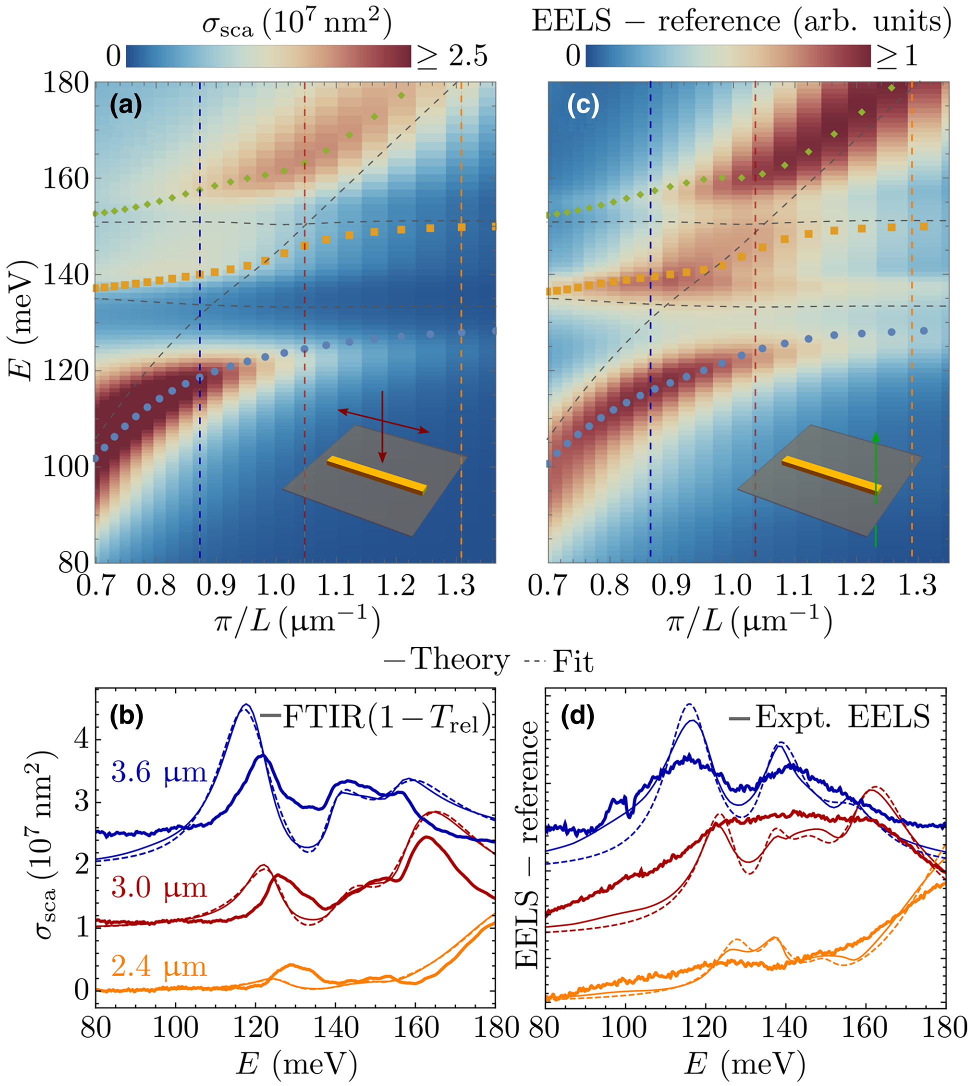

FIG. 3. Coupled system response as a function of the plasmonic antenna length. (a),(b) Optical scattering and (c),(d) reference-subtracted EEL spectra (see Fig. 2 for details). Simulated pseudodispersions in (a) and (c) are obtained via the transformation $k_{\rm LSP} = \pi/L$, where $L$ is the antenna length and $k_{\rm LSP}$ is the effective wave vector of the dipolar LSP. Gray dashed lines trace energies of the uncoupled LSPs and PhPs, whereas the colored symbols denote energies of the new hybrid modes characterized by eigenvalues obtained from fitting of spectra and solution of $|\mathbf{M}| = 0$. Examples of numerically calculated, fitted, and experimental spectra (thin, dashed, and thick curves, respectively) for three selected lengths (2.4, 3.0, 3.6 μm) are shown in (b) and (d) [denoted by vertical colored dashed lines in (a) and (c)]. All EEL spectra are obtained for a 60-keV electron beam placed close to the corner of the antenna [violet line in Fig. 2(c)]. Experimental measurements of EELS and FTIR are performed on the same sample.

Figure 3 shows the dependence of the coupled system response on the parameter controlling the energy of the LSP, which is simply given by the length of the antenna's long axis $L$. Changing the antenna's dimension enables us to analyze the length-dependent coupling strengths $g_i = K_i\sqrt{f_if_{\rm LSP}}/\sqrt{\omega_{{\rm SPhP}_i}\omega_{\rm LSP}}$, where $i = \{1, 2\}$ [48], which can be obtained from fitting the optical scattering cross section and reference-subtracted EEL spectra to analytical models. We find that the overall system spectral response is approximately governed by an effective polarizability

$$\alpha \propto [\mathbf{M}^{-1}]_{11} = \frac{\alpha_{\rm LSP} f}{1 - \sum_{i=1,2} g_i^2 \omega_{{\rm SPhP}_i}\omega_{\rm LSP}\alpha_{{\rm SPhP}_i}\alpha_{\rm LSP}}, \quad (3)$$

where $f$ is an effective response strength, and which indicates that the LSP primarily couples and decouples to the propagating IR photons as well as to the evanescent electromagnetic field supplied by the electron beam. The $[\mathbf{M}^{-1}]_{11}$ term also suggests that the SPhPs are launched secondarily by the antenna.

The scattering cross-section spectra in Figs. 3(a) and 3(b) can then be modeled by [46,47]

$$\sigma_{\rm sca} \approx \frac{k^4}{6\pi\epsilon_0^2}\,|\alpha|^2\,, \quad (4)$$

where $\epsilon_0$ is the permittivity of vacuum and $k = \omega/c$ is the free-space wave vector of light with photon energy $\hbar\omega$ moving at the speed of light $c$. To model the reference-subtracted EEL probabilities in Figs. 3(c) and 3(d), we use [15]

$$\text{EELS} - \text{reference} \approx \mathcal{F}_1(\omega)\text{Im}\{\alpha\} + \mathcal{F}_2(\omega)\text{Im}\{\alpha_{\text{SPhP}_1}\}, \tag{5}$$

where $\mathcal{F}_{1/2}(\omega) = A_{1/2}\omega^{j_{1/2}}$ with $A_x$ and $j_x$ being unknown real fitting parameters representing scaling factors and powers. These spectral functions incorporate an overlap of the plasmonic field with the field of the electron beam. The second term in Eq. (5) captures a residual spectral contribution of the noninteracting SPhPs, which remains even after the reference subtraction. A residual spectral contribution remains because a slightly larger portion of SPhPs (or SPhPs with different momenta) can be excited when the beam is placed close to the antenna's corner. This residue can be clearly seen within the RB in Fig. 3(c) when compared to Fig. 3(a).

Fitting the simulated scattering and the reference-subtracted EEL spectra with models in Eqs. (4) and (5), respectively, allows us to obtain the parameters characterizing the uncoupled system constituents, i.e., the excitations' energies and dampings. The theoretically obtained LSP and SPhP energies are interpolated by the gray dashed lines in Figs. 3(a) and 3(c). We can observe the plasmon energy linearly increasing with the inverse antenna length, which is typical for MIR plasmonic antennas on transparent substrates [49]. Note, however, that energies of both SPhPs remain nearly constant, as expected. The equation $|\mathbf{M}| = 0$ together with the parameters obtained from the model fitting provides the energies of the new hybrid modes, shown as colored symbols. These energies should be close to the actual peak positions, but typically do not coincide perfectly. However, we observe a close correspondence of the coupled system energies obtained for both types of probes.

The simulated spectra are compared with the experimental results for three fabricated antenna lengths in Figs. 3(b) and 3(d). The $(1 - T_{\text{rel}})$ FTIR spectra exhibit decent agreement with the calculated scattering with only slight discrepancies in the observed peak energies and relative strengths. However, it is important to keep in mind that the correspondence of the $(1 - T_{\text{rel}})$ with the scattering cross section is established only empirically; an exact illumination and light collection geometry can play a role (see Appendix A for further discussion). Maybe more importantly, the optical spectra are recorded for an antenna array and thus involve many antennas with various imperfections and divergences with respect to nominal dimensions. On the other hand, each reference-subtracted experimental EEL spectrum in Fig. 3(d) is recorded for an individual antenna within the array and thus does not involve any size averaging, which represents a great advantage of using focused electron probes. However, some of the fine details are hidden due to the current instrumental resolution (see Fig. 6 in Appendix B).

## V. QUANTIFICATION OF THE COUPLING

The fitting enables us to extract the values of the coupling strengths $g_i$ that are key for the classification of the coupling in the system. We theoretically predict and experimentally confirm that a rectangular Au nanoantenna on a $\text{SiO}_2$ substrate can be in a strong coupling regime, supported by the fulfillment of the criterion [50] $2g_i > \gamma_{\text{LSP}} + \gamma_{\text{SPhP}_i}$ for coupling of the LSP with both SPhPs, as documented in Fig. 4, where we find optimal coupling conditions for $L \sim 3.4$ μm. The fits of the optical spectra and reference-subtracted EELS (the latter not shown) provide similar coupling strengths with differences within uncertainties due to fitting errors, which demonstrates that the coupling is determined by the system itself, and is not probe dependent. Moving the electron beam towards the antenna center substantially lowers the overall efficiency of the LSP excitation, and thus the contrast of the spectral features. However, the coupling strengths stay nearly the same except for the beam positioned at the center of the antenna, where we observe a dramatic change of the coupling strengths towards zero as the dipolar LSP cannot be excited anymore.

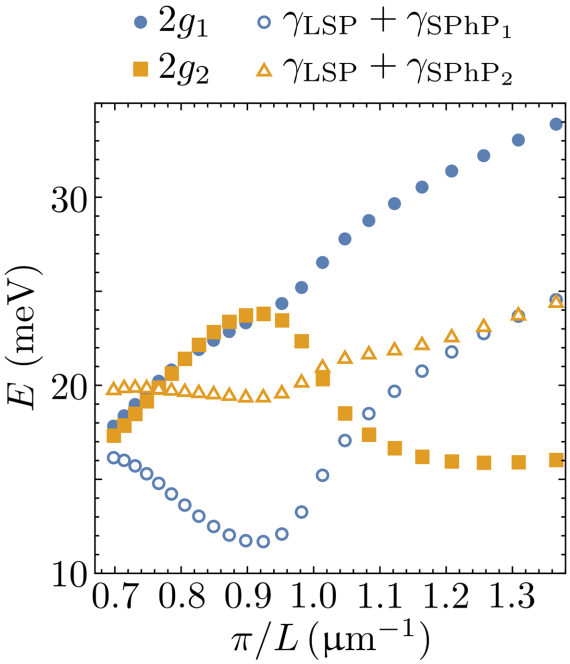

FIG. 4. Coupling parameters compared to their damping extracted from the fitted optical spectra in Fig. 3 (fitting reference-subtracted EEL spectra provides values with a difference within about 1 meV). The criterion $2g_i > \gamma_{\text{LSP}} + \gamma_{\text{SPhP}_i}$ establishes the strong coupling.

## VI. CONCLUSIONS

In conclusion, here we have performed a comparative experimental study of spectra of the coupled antenna-substrate system obtained with far-field light and near-field electron spectroscopy. The study reveals fundamental differences when probing a complex polaritonic system with light and focused electron probes. We show that a precise positioning of the electron beam offers the possibility to probe coupled or uncoupled excitations at will, thus offering complementary information to that obtained from far-field optical spectroscopy.

We also present a postprocessing analysis in the EEL spectra that consists of subtracting a reference from spectra acquired for different beam positions with respect to the nanostructure system to reveal the strength of coupling between phonon and plasmon polariton excitations. The postprocessing facilitates comparison of EEL with far-field optical spectra, from which we find that both techniques can yield nearly identical coupled-system parameters. Such comparison confirms that the coupling is eventually determined by the optical properties and geometry of the system constituents, and should be independent of probing technique. The workflow presented here can be generalized for the study of excitations arising when geometry, topology, and different materials are used to generate hybrid optical systems.

## ACKNOWLEDGMENTS

We acknowledge support from the Czech Science Foundation (Grant No. 20-28573S), European Commission (H2020-Twinning Project No. 810626 - SINNCE, M-ERA NET HYSUCAP/TACR-TH71020004), BUT - specific research No. FSI-S-20-6485, and the Ministry of Education, Youth and Sports of the Czech Republic (CzechNanoLab Research Infrastructure - LM2018110). EELS measurements were supported by the Center for Nanophase Materials Sciences (CNMS), which is a U.S. Department of Energy, Office of Science User Facility. EELS experimental work at ORNL was conducted, in part, using instrumentation within ORNL's Materials Characterization Core provided by UT-Batelle, LLC, under Contract No. DE-AC05-00OR22725 with the U.S. Department of Energy, and sponsored by the Laboratory Directed Research and Development Program of Oak Ridge National Laboratory, managed by UT-Battelle, LLC, for the U.S. Department of Energy. We thank our colleagues Michal Horák, Marek Vaňatka and Vojtěch Švarc for their advice on lithography on TEM membranes.

## APPENDIX A: CORRESPONDENCE BETWEEN EXPERIMENTAL FTIR AND NUMERICALLY CALCULATED SPECTRA

It is well known that experimentally measured optical spectra strongly depend on exact illumination and collection geometry [51]. In our case, the illumination and collection angles are between 15° and 30°; however, we do not know an exact instrument point spread function, which prevents us from perfectly mimicking the experimental setup in the simulations.

Moreover, the collected signal comes from an array of antennas where fabrication imperfections cause averaging over the signal from slightly different antenna sizes (estimated size deviation of about 10 nm) and, maybe more importantly, the antenna edges and surfaces are not perfectly smooth. Our approach thus relies on evaluation of all relevant optical quantities in a standard bright-field illumination geometry, which we then compare with experimentally measured spectra and establish the best correspondence.

Figure 5(a) shows the calculated reflection, absorption, and transmission (or, more precisely, $1 - T$) spectra, whose spectral shapes strongly resemble scattering, absorption, and extinction cross sections, respectively. The experimentally measured spectra on the antenna-SiO$_2$ layer system are, however, normalized with respect to

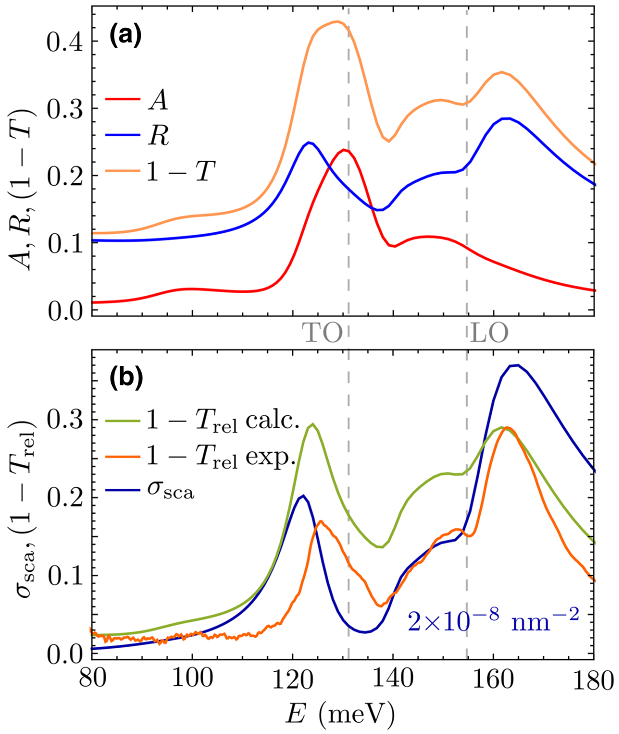

FIG. 5. (a) Comparison of theoretically calculated absorption ($A$, red line), reflection ($R$, blue line), and 1− transmission ($1 - T$, orange line) spectra for the plane-wave excitation and the geometry considered in Fig. 2. (b) Comparison of "relative" transmission spectra ($1 - T_{\rm rel}$) obtained by dividing the total transmission spectra by a reference on a plain SiO$_2$ layer. We show calculated and experimentally measured FTIR spectra (green versus orange lines) together with the calculated scattering cross section (dark blue line).

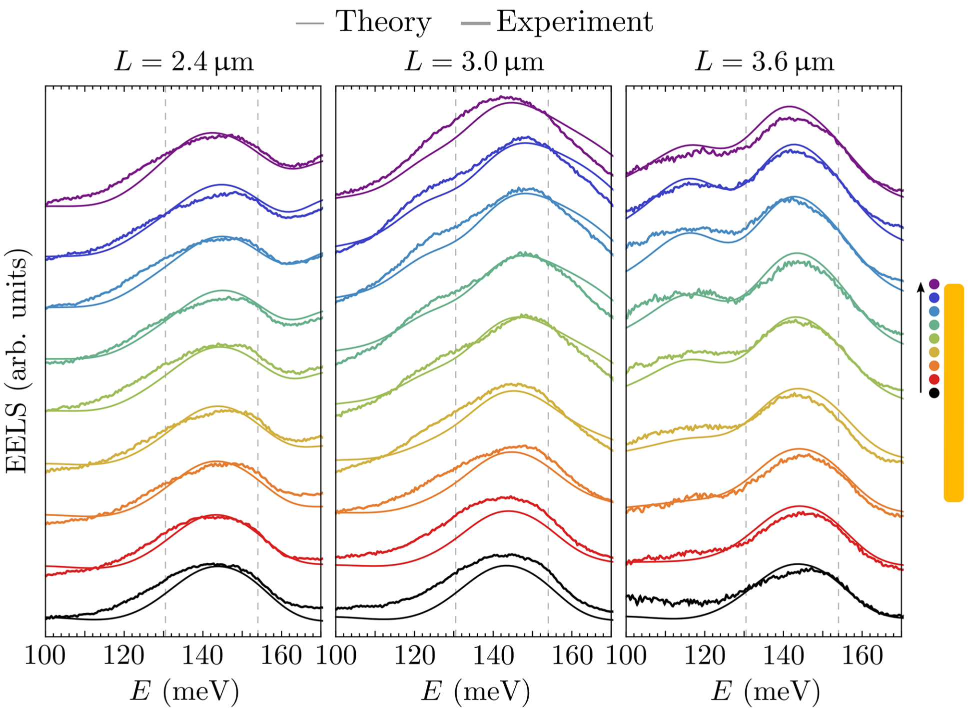

FIG. 6. Comparison of theoretically calculated EEL spectra after convolution with a Gaussian function of 14 meV FWHM (thin lines) with experimentally measured spectra (thick lines) for the varying beam position as shown in the inset and three antenna's lengths.

spectra measured on plain $SiO_2$ membranes. This "relative" experimental transmission spectrum [orange line in Fig. 5(b) and also in Fig. 2(a)] then exhibits a slightly better correspondence with the calculated scattering cross section [blue line in Fig. 5(b)] compared to the calculated relative transmission (green line). Such empirical observation leads us to considering calculated scattering cross sections for the comparison with relative transmission obtained from FTIR measurements.

## APPENDIX B: FINITE SPECTRAL RESOLUTION IN EELS

Figure 6 shows a comparison of the theoretical EEL spectra when convoluted with a Gaussian function of 14 meV FWHM to mimic the energy resolution of the involved STEM-EELS setup.

TABLE I. Bounds for fitting of model parameters.

| Parameter | Lower bound | Upper bound |
|---|---|---|
| $\omega_{\mathrm{SPhP}_1}$ (meV) | 131.9 | 135.6 |
| $\gamma_{\mathrm{SPhP}_1}$ (meV) | 1 | 10 |
| $\omega_{\mathrm{SPhP}_2}$ (meV) | 148 | 154.6 |
| $\gamma_{\mathrm{SPhP}_2}$ (meV) | 2 | 20 |
| $\omega_{\mathrm{LSP}}$ (meV) | 80 | 200 |
| $\gamma_{\mathrm{LSP}}$ (meV) | 1 | 50 |
| $f$ | 1 | 10 |
| $g_1$ (meV) | 1 | 50 |
| $g_2$ (meV) | 1 | 50 |
| $j_1$ | −2 | 3 |
| $j_2$ | −1 | 1.5 |

## APPENDIX C: DETAILS ON FITTING

We use the least-square method and fix parameters within the restricted ranges specified in Table I.

[1] J. D. Caldwell, L. Lindsay, V. Giannini, I. Vurgaftman, T. L. Reinecke, S. A. Maier, and O. J. Glembocki, Low-loss, infrared and terahertz nanophotonics using surface phonon polaritons, Nanophotonics **4**, 44 (2015).

[2] M. I. Stockman, Nanofocusing of Optical Energy in Tapered Plasmonic Waveguides, Phys. Rev. Lett. **93**, 137404 (2004).

[3] A. J. Huber, B. Deutsch, L. Novotny, and R. Hillenbrand, Focusing of surface phonon polaritons, Appl. Phys. Lett. **92**, 203104 (2008).

[4] E. Moreno, S. G. Rodrigo, S. I. Bozhevolnyi, L. Martín-Moreno, and F. J. García-Vidal, Guiding and Focusing of Electromagnetic Fields with Wedge Plasmon Polaritons, Phys. Rev. Lett. **100**, 023901 (2008).

[5] P. Li, M. Lewin, A. V. Kretinin, J. D. Caldwell, K. S. Novoselov, T. Taniguchi, K. Watanabe, F. Gaussmann, and T. Taubner, Hyperbolic phonon-polaritons in boron nitride for near-field optical imaging and focusing, Nat. Commun. **6**, 1 (2015).

[6] S. Dai, Z. Fei, Q. Ma, A. S. Rodin, M. Wagner, A. S. McLeod, M. K. Liu, W. Gannett, W. Regan, K. Watanabe, T. Taniguchi, M. Thiemens, G. Dominguez, A. H. C. Neto, A. Zettl, F. Keilmann, P. Jarillo-Herrero, M. M. Fogler, and D. N. Basov, Tunable phonon polaritons in atomically thin van der Waals crystals of boron nitride, Science **343**, 1125 (2014).

[7] G. Spektor, A. David, B. Gjonaj, G. Bartal, and M. Orenstein, Metafocusing by a metaspiral plasmonic lens, Nano Lett. **15**, 5739 (2015).

[8] M. Autore, P. Li, I. Dolado, F. J. Alfaro-Mozaz, R. Esteban, A. Atxabal, F. Casanova, L. E. Hueso, P. Alonso-González, J. Aizpurua, A. Y. Nikitin, S. Vélez, and R. Hillenbrand, Boron nitride nanoresonators for phonon-enhanced molecular vibrational spectroscopy at the strong coupling limit, Light Sci. Appl. **7**, 17172 (2018).

[9] U. Hohenester, *Nano and Quantum Optics* (Springer Nature Switzerland, Cham, 2020).

[10] E. Prodan, C. Radloff, N. J. Halas, and P. Nordlander, Hybridization model for the plasmon response of complex nanostructures, Science **302**, 419 (2003).

[11] P. Nordlander, C. Oubre, E. Prodan, K. Li, and M. I. Stockman, Plasmon hybridizaton in nanoparticle dimers, Nano Lett. **4**, 899 (2004).

[12] C. Cherqui, Y. Wu, G. Li, S. C. Quillin, J. A. Busche, N. Thakkar, C. A. West, N. P. Montoni, D. Rack, J. P. Camden, and D. J. Masiello, STEM/EELS imaging of magnetic hybridization in symmetric and symmetry-broken plasmon oligomer dimers and all-magnetic Fano interference, Nano Lett. **16**, 6668 (2016).

[13] S. C. Quillin, C. Cherqui, N. P. Montoni, G. Li, J. P. Camden, and D. J. Masiello, Imaging plasmon hybridization in metal nanoparticle aggregates with electron energy-loss spectroscopy, J. Phys. Chem. C **120**, 20852 (2016).

[14] A. B. Yankovich, B. Munkhbat, D. G. Baranov, J. Cuadra, E. Olsén, H. Lourenço-Martins, L. H. G. Tizei, M. Kociak, E. Olsson, and T. Shegai, Visualizing spatial variations of plasmon–exciton polaritons at the nanoscale using electron microscopy, Nano Lett. **19**, 8171 (2019).

[15] K. C. Smith, A. Olafsson, X. Hu, S. C. Quillin, J. C. Idrobo, R. Collette, P. D. Rack, J. P. Camden, and D. J. Masiello, Direct Observation of Infrared Plasmonic Fano Antiresonances by a Nanoscale Electron Probe, Phys. Rev. Lett. **123**, 177401 (2019).

[16] V. Křápek, A. Konečná, M. Horák, F. Ligmajer, M. Stöger-Pollach, M. Hrtoň, J. Babocký, and T. Šikola, Independent engineering of individual plasmon modes in plasmonic dimers with conductive and capacitive coupling, Nanophotonics **9**, 623 (2020).

[17] G. Lu, C. R. Gubbin, J. R. Nolen, T. Folland, M. J. Tadjer, S. De Liberato, and J. D. Caldwell, Engineering the spectral and spatial dispersion of thermal emission via polariton–phonon strong coupling, Nano Lett. **21**, 1831 (2021).

[18] T. Šikola, R. D. Kekatpure, E. S. Barnard, J. S. White, P. Van Dorpe, L. Břínek, O. Tomanec, J. Zlámal, D. Y. Lei, Y. Sonnefraud, S. A. Maier, J. Humlíček, and M. L. Brongersma, Mid-IR plasmonic antennas on silicon-rich oxinitride absorbing substrates: Nonlinear scaling of resonance wavelengths with antenna length, Appl. Phys. Lett. **95**, 253109 (2009).

[19] C. Huck, J. Vogt, T. Neuman, T. Nagao, R. Hillenbrand, J. Aizpurua, A. Pucci, and F. Neubrech, Strong coupling between phonon-polaritons and plasmonic nanorods, Opt. Express **24**, 25528 (2016).

[20] P. Pons-Valencia, F. J. Alfaro-Mozaz, M. M. Wiecha, V. Biolek, I. Dolado, S. Vélez, P. Li, P. Alonso-González, F. Casanova, L. E. Hueso, L. Martín-Moreno, R. Hillenbrand, and A. Y. Nikitin, Launching of hyperbolic phonon-polaritons in h-BN slabs by resonant metal plasmonic antennas, Nat. Commun. **10**, 1 (2019).

[21] L. Břínek, M. Kvapil, T. Šamořil, M. Hrtoň, R. Kalousek, V. Křápek, J. Spousta, P. Dub, P. Varga, and T. Šikola, Plasmon resonances of mid-IR antennas on absorbing substrate: Optimization of localized plasmon-enhanced absorption upon strong coupling effect, ACS Photonics **5**, 4378 (2018).

[22] R. Hillenbrand, T. Taubner, and F. Keilmann, Phonon-enhanced light-matter interaction at the nanometer scale, Nature **418**, 159 (2002).

[23] O. L. Krivanek, T. C. Lovejoy, N. Dellby, T. Aoki, R. W. Carpenter, P. Rez, E. Soignard, J. Zhu, P. E. Batson, M. J. Lagos, R. F. Egerton, and P. A. Crozier, Vibrational spectroscopy in the electron microscope, Nature **514**, 209 (2014).

[24] R. F. Egerton, *Electron Energy-Loss Spectroscopy in the Electron Microscope* (Plenum Press, New York, 1996).

[25] M. J. Lagos, A. Trügler, U. Hohenester, and P. E. Batson, Mapping vibrational surface and bulk modes in a single nanocube, Nature **543**, 529 (2017).

[26] A. A. Govyadinov, A. Konečná, A. Chuvilin, S. Vélez, I. Dolado, A. Y. Nikitin, S. Lopatin, F. Casanova, L. E. Hueso, J. Aizpurua, and R. Hillenbrand, Probing low-energy hyperbolic polaritons in van der Waals crystals with an electron microscope, Nat. Commun. **8**, 1 (2017).

[27] A. Konečná, K. Venkatraman, K. March, P. A. Crozier, R. Hillenbrand, P. Rez, and J. Aizpurua, Vibrational electron energy loss spectroscopy in truncated dielectric slabs, Phys. Rev. B **98**, 205409 (2018).

[28] L. H. G. Tizei, V. Mkhitaryan, H. Lourenço-Martins, L. Scarabelli, K. Watanabe, T. Taniguchi, M. Tencé, J. D. Blazit, X. Li, A. Gloter, A. Zobelli, F. P. Schmidt, L. M. Liz-Marzán, F. J. García de Abajo, O. Stéphan, and M. Kociak, Tailored nanoscale plasmon-enhanced vibrational electron spectroscopy, Nano Lett. **20**, 2973 (2020).

[29] H. Yang, E. L. Garfunkel, and P. E. Batson, Probing free carrier plasmons in doped semiconductors using spatially resolved electron energy loss spectroscopy, Phys. Rev. B **102**, 205427 (2020).

[30] N. Li, X. Guo, X. Yang, R. Qi, T. Qiao, Y. Li, R. Shi, Y. Li, K. Liu, Z. Xu, L. Liu, F. J. García de Abajo, Q. Dai, E.-G. Wang, and P. Gao, Direct observation of highly confined phonon polaritons in suspended monolayer hexagonal boron nitride, Nat. Mater. **20**, 43 (2020).

[31] A. Konečná, J. Li, J. H. Edgar, F. J. García de Abajo, and J. A. Hachtel, Revealing nanoscale confinement effects on hyperbolic phonon polaritons with an electron beam, Small **17**, 2103404 (2021).

[32] M. J. Lagos, P. E. Batson, Z. Lyu, and U. Hohenester, Imaging strongly coupled plasmon–phonon modes in mid-infrared double antennas, ACS Photonics **8**, 1293 (2021).

[33] Ansys Lumerical inc. www.lumerical.com.

[34] Comsol Multiphysics, www.comsol.com.

[35] F. J. García de Abajo, Optical excitations in electron microscopy, Rev. Mod. Phys. **82**, 209 (2010).

[36] J. A Hachtel, A. R. Lupini, and J. C. Idrobo, Exploring the capabilities of monochromated electron energy loss spectroscopy in the infrared regime, Sci. Rep. **8**, 5637 (2018).

[37] T. Lovejoy, G. Corbin, N. Dellby, M. Hoffman, and O. L. Krivanek, Advances in ultra-high energy resolution STEM-EELS., Microsc. Microanal. **24**, 446 (2018).

[38] J. Kischkat, S. Peters, B. Gruska, M. Semtsiv, M. Chashnikova, M. Klinkmüller, O. Fedosenko, S. Machulik, A. Aleksandrova, G. Monastyrskyi, Y. Flores, and W. T. Masselink, Mid-infrared optical properties of thin films of aluminum oxide, titanium dioxide, silicon dioxide, aluminum nitride, and silicon nitride, Appl. Opt. **51**, 6789 (2012).

[39] E. D. Palik, *Handbook of Optical Constants of Solids* (Academic Press, San Diego, 1985).

[40] R. Fuchs and K. L. Kliewer, Optical modes of vibration in an ionic crystal slab, Phys. Rev. **140**, A2076 (1965).

[41] K. Venkatraman, P. Rez, K. March, and P. A Crozier, The influence of surfaces and interfaces on high spatial resolution vibrational EELS from $SiO_2$, Microscopy **67**, i14 (2018).

[42] Y.-H. Li, M. Wu, R.-S. Qi, N. Li, Y.-W. Sun, C.-L. Shi, X.-T. Zhu, J.-D. Guo, D.-P. Yu, and P. Gao, Probing lattice vibrations at $SiO_2$/Si surface and interface with nanometer resolution, Chin. Phys. Lett. **36**, 026801 (2019).

[43] A. A. Lucas and E. Kartheuser, Energy-loss spectrum of fast electrons in a dielectric slab. I. Nonretarded losses and Cherenkov bulk loss, Phys. Rev. B **1**, 3588 (1970).

[44] D. Rossouw, M. Couillard, J. Vickery, E. Kumacheva, and G. A. Botton, Multipolar plasmonic resonances in silver nanowire antennas imaged with a subnanometer electron probe, Nano Lett. **11**, 1499 (2011).

[45] A. Konečná, T. Neuman, J. Aizpurua, and R. Hillenbrand, Surface-enhanced molecular electron energy loss spectroscopy, ACS Nano **12**, 4775 (2018).

[46] S. Albaladejo, R. Gómez-Medina, L. S. Froufe-Pérez, H. Marinchio, R. Carminati, J. F. Torrado, G. Armelles, A. García-Martín, and J. J. Sáenz, Radiative corrections to the polarizability tensor of an electrically small anisotropic dielectric particle, Opt. Express **18**, 3556 (2010).

[47] E. Castanié, R. Vincent, R. Pierrat, and R. Carminati, Absorption by an optical dipole antenna in a structured environment, Int. J. Opt. **2012**, 452047 (2012).

[48] L. Novotny, Strong coupling, energy splitting, and level crossings: A classical perspective, Am. J. Phys. **78**, 1199 (2010).

[49] Y. Wu, Z. Hu, X.-T. Kong, J. C. Idrobo, A. G. Nixon, P. D. Rack, D. J. Masiello, and J. P. Camden, Infrared plasmonics: STEM-EELS characterization of Fabry-Pérot resonance damping in gold nanowires, Phys. Rev. B **101**, 085409 (2020).

[50] P. Törmä and W. L. Barnes, Strong coupling between surface plasmon polaritons and emitters: A review, Rep. Prog. Phys. **78**, 013901 (2014).

[51] M. W. Knight, J. Fan, F. Capasso, and N. J. Halas, Influence of excitation and collection geometry on the dark field spectra of individual plasmonic nanostructures, Opt. Express **18**, 2579 (2010).